mater.scichina.com link.springer.com

Published online 5 January 2023 | https://doi.org/10.1007/s40843-022-2299-6
Sci China Mater 2023, 66(5): 2079–2089

Controlled synthesis of highly stable lead-free bismuth halide perovskite nanocrystals: Structures and photophysics

Huifang Geng[1†], Zhuanzhuan Huang[1†], Huaxiu Geng[2], Siyu Liu[1], Maria A Naumova[3], Raffaele Salvia[4], Siqi Chen[5], Junli Wei[5], Lifu Zhang[1], Xianshao Zou[6], Weihua Lin[6], Xinyi Cai[7], Mingjian Yuan[5], Zhenpeng Hu[1], Xi Shen[8], Richeng Yu[8], Kaibo Zheng[6,9*], Sophie E. Canton[9*] and Xuewen Fu[1,10*]

ABSTRACT **Recently, cesium bismuth halide perovskites have emerged as potential substitutes to their counterparts, cesium lead halide perovskites, owing to their low toxicity. However, the photophysics of cesium-bismuth halides nanocrystals (NCs) have not yet been fully rationalized because their structures remain highly debated. The ultraviolet-visible (UV-vis) absorption along with other photophysical properties such as the nature and lifetime of the excited states vary considerably across the previous reports. Here, we successfully synthesize pure Cs_3BiBr_6 and $Cs_3Bi_2Br_9$ NCs *via* a modified hot-injection method, where the structure can be easily controlled by tuning the reaction temperature. The UV-vis absorption spectrum of the pure $Cs_3Bi_2Br_9$ NCs features two characteristic peaks originating from the absorption of the first exciton and second exciton, respectively, which ultimately clarifies the debate in the previous reports. Using femtosecond transient absorption spectroscopy, we systematically investigate the excited state dynamics of the $Cs_3Bi_2Br_9$ NCs and reveal that the photoexcited carriers undergo a self-trapping process within 3 ps after excitation. More intriguingly, the $Cs_3Bi_2Br_9$ NCs prepared by this method show much better photostability than those prepared by the ligand-assisted reprecipitation process. Photodetectors based on these $Cs_3Bi_2Br_9$ NCs show a sensitive light response, demonstrating the definite potential for breakthrough optoelectronic applications.**

Keywords: lead-free perovskites, bismuth perovskites, nanocrystals, hot injection, photostability

INTRODUCTION

Metal halide perovskites (MHP) are considered among the most promising materials in the field of optoelectronics as they combine a wealth of superior physicochemical properties. In particular, lead-based MHP with flexible inorganic lattice presents a high absorption coefficient, high fluorescence quantum yield, tunable bandgap throughout the visible spectrum, long carrier diffusion length, and high carrier mobility [1–8]. All these attributes greatly favor their intensive integration into optoelectronic devices such as solar cells, photoelectric diodes, photoelectric detectors, and lasers [9–14]. However, the toxicity of lead poses a great threat to the environment and human health, making their use in consumer optoelectronics a major hurdle [15,16]. To overcome this challenge, lead-free MHPs gradually came to the public eye and consequent studies on the replacement of Pb^{2+} by other metal cations, such as Ge^{2+}, Sn^{2+}, Bi^{3+}, Sb^{3+} and Ag^{+}, have been widely reported [17–20]. Since trivalent Bi^{3+} is isoelectronic with Pb^{2+} and inorganic perovskites are much more stable than their organic analogs, the all-inorganic cesium bismuth-based MHPs have recently received a particular rush of interest [21]. Cesium bismuth-based halide perovskites possess diverse structures, of which most attention has been focused on $Cs_3Bi_2Br_9$ [22–26]. The interest has recently propagated toward the field of photocatalysis, where the light-harvesting capabilities of $Cs_3Bi_2Br_9$ are utilized for driving chemical reactions with high yields [24,27–29].

Bulk $Cs_3Bi_2Br_9$ is a two-dimensional layered vacancy-ordered perovskite having a trigonal crystalline structure with *P*-3*m*1 symmetry, which can be viewed as a triplication of the traditional ABX_3 unit cell with only two-thirds of the B sites fully

[1] Ultrafast Electron Microscopy Laboratory, Key Laboratory of Weak-Light Nonlinear Photonics (Ministry of Education), School of Physics, Nankai University, Tianjin 300071, China
[2] Institute of Molecular Plus, Tianjin University, Tianjin 300072, China
[3] Deutsches Elektronen-Synchrotron DESY, Notkestr. 85, 22607 Hamburg, Germany
[4] Scuola Normale Superiore, Piazza dei Cavalieri 7, IT-56126 Pisa (PI), Italy
[5] Key Laboratory of Advanced Energy Materials Chemistry (Ministry of Education), Renewable Energy Conversion and Storage Center (RECAST), College of Chemistry, Nankai University, Tianjin 300071, China
[6] Chemical Physics and Nano Lund, Lund University, Box 124, 22100 Lund, Sweden
[7] Binhai College, Nankai University, Tianjin 300270, China
[8] Beijing National Laboratory for Condensed Matter Physics, Institute of Physics, Chinese Academy of Sciences, Beijing 100190, China
[9] Department of Chemistry, Technical University of Denmark, DK-2800 Kongens Lyngby, Denmark
[10] Collaborative Innovation Center of Extreme Optics, Shanxi University, Taiyuan 030006, China
[†] These authors contributed equally to this work.
[*] Corresponding authors (emails: xwfu@nankai.edu.cn (Fu X); sophie.canton@xfel.eu or socant@kemi.dtu.dk (Canton SE); kaibo.zheng@chemphys.lu.se (Zheng K))

occupied by Bi^{3+} [30,31]. Hitherto, numerous articles have reported the preparation and the photophysics of $Cs_3Bi_2Br_9$ nanocrystals (NCs) [25,32–36]. However, the published optical absorption spectra of $Cs_3Bi_2Br_9$ NCs vary significantly (see the plot showing the wavelengths of the peak maxima as a function of the particle size in Fig. S1). For example, Yang *et al.* [25] synthesized blue light-emitting $Cs_3Bi_2Br_9$ NCs with a size of 6 nm by a ligand-assisted re-precipitation (LARP) method, where isopropanol was used as the antisolvent during the synthesis. The absorption spectrum of the $Cs_3Bi_2Br_9$ NCs shows a pronounced peak at 439 nm and the photoluminescence quantum yield (PLQY) of 0.2% without capping ligands and 4.5% with capping ligands. Leng *et al.* [32] produced $Cs_3Bi_2Br_9$ NCs with an average diameter of 3.88 ± 0.67 nm and a PLQY of up to 19.4% by the similar LARP method, where ethanol was used as the antisolvent and a peak centered at 396 nm was observed in their absorption spectrum. In the same year, Lou *et al.* [34] reported $Cs_3Bi_2Br_9$ NCs dispersed in octane with an average diameter of 3.5 nm *via* the LARP reaction, and their NCs showed a sharp ultraviolet-visible (UV-vis) peak at 371 nm in the absorption spectrum and exhibited a strong blue-violet emission under UV light irradiation with a PLQY of up to 22%. It can be seen that the peaks in the absorption spectra of the $Cs_3Bi_2Br_9$ NCs exhibit a blueshift as the size of NCs decreases. However, Cao *et al.* [33] reported a striking blueshifted absorption peak at 330 nm for 4.8 nm $Cs_3Bi_2Br_9$ NCs dispersed in ethanol with a PLQY up to 37% by a modified LARP method, which does not follow the correlation stated above. In addition to the LARP method, many alternative synthetic approaches have also been tried to synthesize $Cs_3Bi_2Br_9$ NCs. For example, Yang *et al.* [35] used a metal ion insertion procedure to make 13 nm $Cs_3Bi_2Br_9$ NCs, which showed an absorbance peak at 430 nm. Nelson *et al.* [36] prepared $Cs_3Bi_2Br_9$ NCs with an absorption peak at 380 nm by hot injection, but the size of the NCs was ~20 nm, which is too large for quantum confinement to manifest. In other words, quantum confinement can be ruled out as being the reason for the high energy position of this peak. Another published study on $Cs_3Bi_2Br_9$ NCs also reports a sharp absorption peak at 380 nm, but with even larger sizes [26]. Overall, strong disparities clearly exist among the peak positions of the $Cs_3Bi_2Br_9$ NCs, so that, to date, the assignment of the absorption spectra has not been firmly established yet. This survey suggests that the irregularities in trends may be due to unexpected variations in NC size and phase-purity. Resolving this outstanding issue is crucial for the optimization of the nano-objects synthesized from this material as their properties are strongly affected by these parameters.

In this work, we present a modified hot injection (MHI) approach for preparing highly photostable lead-free bismuth perovskite NCs with controllable size and pure phase. As a first step, we show that the composition of the perovskite NCs can be easily regulated by altering the reaction temperature. Between 160 and 180°C, we get pure Cs_3BiBr_6 NCs with a mean particle size of 13.23 ± 0.29 nm. With injection temperatures ranging from 200 to 240°C, we obtain pure $Cs_3Bi_2Br_9$ NCs. The structures of the phase-pure Cs_3BiBr_6 NCs and $Cs_3Bi_2Br_9$ NCs are concurrently confirmed by X-ray diffraction (XRD), Raman spectroscopy, and X-ray absorption spectroscopy (XAS). Cs_3BiBr_6 NCs show a strong absorption peak at 380 nm. While $Cs_3Bi_2Br_9$ NCs feature two absorption peaks, a sharp one between 430 and 440 nm (P1), and a weak one at the wavelength shorter than 400 nm (P2). Our results ultimately clarify the controversy on the absorption peaks of the previously reported $Cs_3Bi_2Br_9$ NCs, which is mainly due to the coexisting phase of Cs_3BiBr_6 NCs. As a second step, we concentrate on the properties of the phase-pure $Cs_3Bi_2Br_9$ NCs produced by our MHI method. We obtain $Cs_3Bi_2Br_9$ NCs with different crystallographic orientations by adjusting the amount of oleic acid (OA), and we control the particle size of the $Cs_3Bi_2Br_9$ NCs by changing the centrifugation speed. Through the absorption spectroscopy measurements on the NCs with different sizes and crystallographic orientations, we find that the absorption peak P2 is tightly linked to the size and the preferred crystallographic orientation of the NCs, while the absorption peak P1 is only size-dependent. Further femtosecond transient absorption (fs-TA) spectroscopy measurements (pumped at 340 nm under various fluences) reveal that the carrier dynamics of the $Cs_3Bi_2Br_9$ NCs (16.00 ± 0.24 nm) shows a rapid trapping process of the photoexcited carriers in the initial ~3 ps. Finally, we demonstrate that photodetectors based on the 16.00 ± 0.24 nm $Cs_3Bi_2Br_9$ NCs show a sensitive light response and a photocurrent enhancement (on/off ratio) of ~43, demonstrating the potential of the MHI $Cs_3Bi_2Br_9$ NCs for breakthrough optoelectronic applications.

EXPERIMENTAL SECTION

Materials

$BiBr_3$ (99%, Aladdin), BiI_3 (99%, Heowins), $BiCl_3$ (98%, Heowins), cesium carbonate (Cs_2CO_3, 99.9%, sigma-aldrich), 1-octadecene (ODE, 90%, Aladdin), OA (90%, Heowins), oleylamine (OLA, 95%, Heowins), and toluene (≥98%, Sinopharm Chemical Reagent Co., Ltd, China) were used without further purification.

Synthesis of Cs-oleate

Cs_2CO_3 (1.628 g) was placed in a 50-mL three-neck flask along with 20 mL ODE and 5 mL OA, dried under vacuum at 120°C for 1 h, and then heated to 150°C under argon until all the Cs_2CO_3 reacted with OA. The Cs-oleate must be preheated to 120°C before use, as it precipitates from ODE at room temperature.

Synthesis of lead-free bismuth perovskite NCs

A mixture of 10 mL ODE, 1 mL OLA, 1 mL OA, 0.05 mL HBr, and 0.376 mmol $BiBr_3$ was placed in a three-neck flask and degassed under vacuum for 1 h at 120°C. Then, the temperature was raised to the indicated temperature (for Cs_3BiBr_6 160–180°C; for $Cs_3Bi_2Br_9$ 200–240°C) under argon atmosphere, and 0.8 mL Cs-oleate solution was briskly added with vigorous stirring. The color of the solution instantly changed to bright yellow-green. In 5 s, the mixture was quenched with an ice water bath.

Purification was carried out with two-round centrifugations. In the first round, the solution was centrifuged at 7000 r min^{-1} for 10 min to collect the precipitate which was then redispersed in 10 mL toluene. Centrifugation was again performed at 7000 r min^{-1} for 5 min for the second round. The yellow-green supernatant was obtained by discarding the bottom precipitates.

For the synthesis of $Cs_3Bi_2Cl_9$ and $Cs_3Bi_2I_9$, the processes are almost the same except that $BiBr_3$ is replaced by $BiCl_3$ and BiI_3, respectively.

Characterization

Transmission electron microscopy (TEM) images, including TEM bright field images and high-resolution TEM (HRTEM), were performed on Talos F200X G2 from FEI Company with the acceleration voltage of 200 kV.

Powder XRD was performed on a Bruker-D8 ADVANCE diffractometer equipped with Cu Kα X-ray tubes (λ = 1.54186 Å) operating at 40 kV and 40 mA. Samples were obtained by slow evaporation of the solvent on a cleaned glass at room temperature.

UV-vis absorption spectra were recorded using the Shimadzu UV-2600. Steady-state fluorescence spectra were recorded using a Shimadzu RF-6000 spectrofluorometer with excitation at 340 nm. PLQY was measured using an FLS 920P steady-state/transient fluorescence spectrometer equipped with an integrating sphere. TRPL spectra were measured using a picosecond pulsed laser (FLS980) with a lase under a repetition rate of 800 kHz at 355 nm. Time-resolved signals were recorded by a time-correlated single photon counting (TCSPC) module with an instrumental total response function (IRF) of less than 100 ps.

LabRAM HR Evolution Raman microscope from HORIBA Scientific was used to obtain the Raman spectra of various samples. The backscattered light was collected, and the Rayleigh scattering peak was filtered using a high-performance Raman edge filter. The final result is a spectrum that displays the intensity of the inelastically scattered light in wavenumbers relative to the wavelength of the exciting laser. The wavelength of excitation is 532 nm.

XAS were acquired at the P64 beamline of Petra III, Deutsches Elektronen-Synchrotron (DESY), Hamburg. Si(311) monochromator crystal and 3rd harmonic of the undulator were used. Higher harmonics rejection was done with two Rh-coated bent mirrors, which additionally focused the beam to the size of 236 μm (hor.) × 77 μm (ver.). Solutions of Cs_3BiBr_6 and $Cs_3Bi_2Br_9$ NCs in toluene were filled into quartz capillaries with 2 mm diameter and positioned into the X-ray beam. Data were acquired in a total fluorescence yield mode using a passivated implanted planar silicon (PIPS) detector. Spectra were taken in a continuous scanning mode. Several X-ray absorption near edge structure (XANES) scans around the Br K-edge (13,474, −50 to 100 eV) were performed; no damage was observed from scan to scan, so the scans were averaged. In the same way, several scans around the Bi L3 edge were averaged. Since the Bi L3 edge (13,419 eV) is only 55 eV below the Br K-edge, the spectra were taken for −50 to 45 eV around the edge. No changes were observed from scan to scan.

TA measurements were performed with the HARPIA-TA spectroscopy system, which is a part of the HARPIA system (HARPIA, light conversion). The light source of HARPIA-TA is a femtosecond laser (Spirit-NOPA, SPECTRA-PHYSICS) operating at 1030 nm and delivering pulses of 170 fs at a repetition rate of 50 kHz. The fundamental laser was split into two beams. One was used to pump an optical parametric amplifier system (OPA, light conversion), and the output of the OPA was used as the pump light of the HARPIA-TA. The other was used to generate white supercontinuum light from a thin Ti:sapphire plate, which was further used as probe light for differential absorption measurements. The probe was time delayed with respect to the pump by a mechanical delay stage. The measurements were performed at room temperature in the air. The pump wavelength was 340 nm, the spot size was 500 μm, and the repetition rate was 6 kHz.

Photodetector fabrication and characterizations

The $Cs_3Bi_2Br_9$ photodetector was fabricated using the indium tin oxide (ITO)/poly(3,4-ethylenedioxythiophene):poly(4-styrenesulfonate) (PEDOT:PSS)/$Cs_3Bi_2Br_9$ NCs/TPBi/LiF/Al sandwich structure. The ITO substrates were sonicated in acetone, ethanol, and deionized water for 15 min each. After drying with nitrogen, the ITO substrates were treated with an oxygen plasma cleaner at 80 W for 5 min to obtain cleaned ITO. A thin layer of PEDOT:PSS was applied to the cleaned ITO surface by spin coating. After the substrates were annealed at 150°C for 10 min, they were transferred to a glovebox filled with nitrogen (<0.01 ppm O_2 and H_2O). The $Cs_3Bi_2Br_9$ NCs dispersed in toluene were spin-coated onto the PEDOT:PSS film at 4000 r min^{-1} for 30 s and then annealed at 100°C (on a hot plate) for 10 min. Then the film was transferred to a thermal evaporator. TPBi (20 nm), LiF (1 nm), and Al (100 nm) were deposited by thermal evaporation with a vacuum pressure under 2×10^{-6} mbar (1 bar = 10^5 Pa). The output electrical characteristics of the device were measured under ambient air conditions.

RESULTS AND DISCUSSION

The present synthesis of lead-free bismuth perovskite NCs using the hot injection method builds on the experience gained from the successful synthesis of $CsPbX_3$ (X = Cl, Br, I) colloidal NCs [37]. The mechanism of perovskite NCs synthesized by hot injection can be found elsewhere. Briefly, the preheated Cs-oleate is injected into the solution containing BX_n (B = Pb^{2+}, Sn^{4+} or Bi^{3+}; X = Cl^-, Br^- or I^-; n = 2, 4 or 3) salt at a specific temperature and then the NCs of a certain size are obtained by quenching in an ice-water bath [38]. In our case, a solution of $BiBr_3$ in ODE with OLA, OA, and hydrobromic acid (HBr) was injected with Cs-oleate at an elevated temperature (160–240°C) (see details in the EXPERIMENTAL SECTION). The scheme of the synthesis method is shown in Fig. 1. In this synthesis, the addition of HBr is another key factor. If HBr was not added to the reaction solution, $BiBr_3$ would reduce to gray metallic Bi at high temperatures before the injection of Cs-oleate [39]. It is noted that the crystal composition can be easily controlled by changing the injection temperature. At a temperature between 160 and 180°C, we obtained colorless colloidal NCs (see Fig. S2a), which turned out to be pure Cs_3BiBr_6 NCs with monoclinic phase, showing isolated $[BiBr_6]^{3-}$ octahedra (see Fig. 1) [40]. The crystal structure of the Cs_3BiBr_6 NCs will be discussed in the following section. When the temperature was set between 200 and 240°C, pure yellowish-green $Cs_3Bi_2Br_9$ NCs were obtained (see Fig. S2b). The sizes of the NCs did not change substantially as the temperature raised, keeping within a range from 16 to 20 nm. Our density functional theory calculations (DFT) predict that the formation of Cs_3BiBr_6 is more favorable than that of $Cs_3Bi_2Br_9$ due to the higher formation energy of the latter one (see Computational details in Supplementary information). Thus, the Cs_3BiBr_6 NCs can be easily obtained at lower temperatures. Intriguingly, the morphology of $Cs_3Bi_2Br_9$ can be further modified by adjusting the amount of OA. For example, products of $Cs_3Bi_2Br_9$ NCs and nanoplatelets can be obtained with 1 and 5 mL OA, respectively. This point will be discussed in detail in the following section.

We first characterized the morphology of the bismuth halide

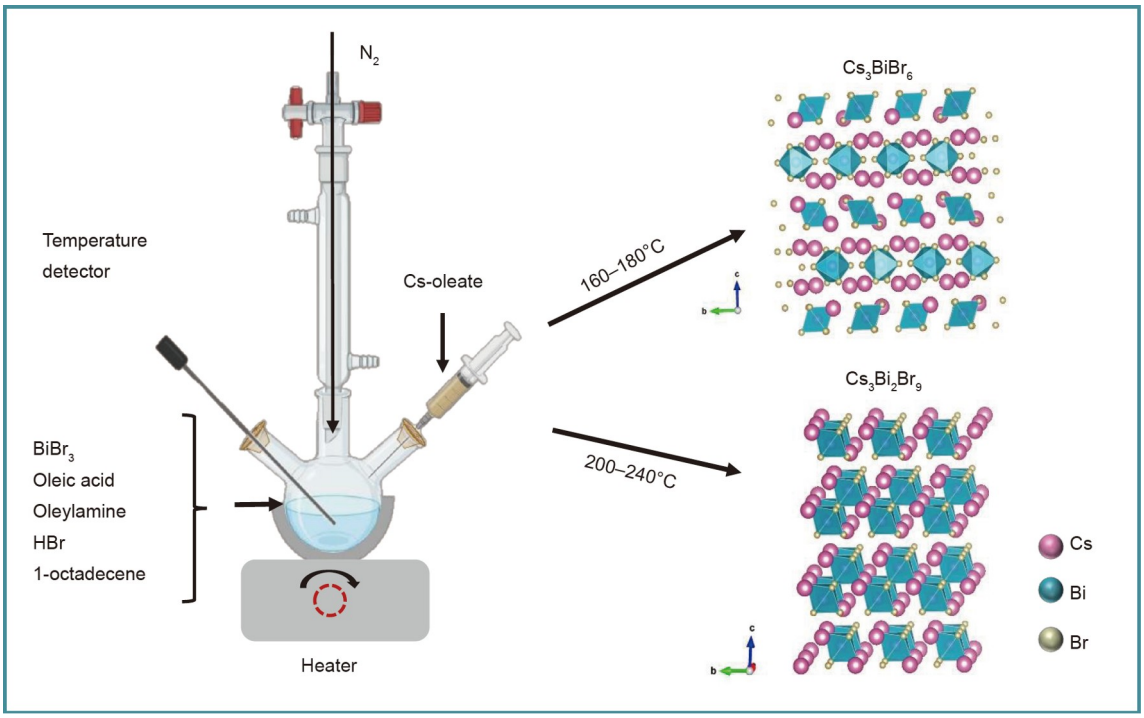

Figure 1 Schematic of the MHI method for the synthesis of colloidal Cs_3BiBr_6 NCs and $Cs_3Bi_2Br_9$ NCs. The crystal structures are produced by VESTA [41].

perovskite NCs by TEM. Fig. 2a, b show the typical bright field TEM images of the as-synthesized Cs_3BiBr_6 NCs (temp 160°C) and $Cs_3Bi_2Br_9$ NCs (temp 200°C), respectively. Both samples exhibit a hexagonal shape. The Cs_3BiBr_6 NCs have a mean particle size of 13.23 ± 0.29 nm, while the $Cs_3Bi_2Br_9$ NCs have a mean particle size of 16.00 ± 0.24 nm. The mean particle size was obtained by fitting the size distribution with a Gaussian function (Fig. S3). The fitted parameters are shown in Table S1. The HRTEM images (insets of Fig. 2a, b) reveal their high crystallinity with a lattice spacing of 0.305 nm corresponding to the (245) plane for Cs_3BiBr_6 NCs and 0.282 nm corresponding to the (202) plane for $Cs_3Bi_2Br_9$ NCs. The crystal structures of these two kinds of perovskite NCs were further confirmed by XRD. Fig. 2c shows the XRD pattern of Cs_3BiBr_6 NCs, in which the numerous peaks are due to the low symmetry of the monoclinic phase within the space group *C*12/*c*1, and the XRD pattern features three groups of peaks clearly at 12°, 20°, and 30°. The result matches well with the previous report [42]. Fig. 2d shows the diffraction pattern of $Cs_3Bi_2Br_9$ NCs. It is well indexed to the standard trigonal perovskite structure (PDF#44-0714) without any visible by-products such as $BiBr_3$. The XRD pattern exhibits peaks at 12.838°, 15.689°, 18.009°, 22.189°, 27.160°, 31.681°, 35.461°, 38.832°, 45.243°, and 56.004°, corresponding to (100), (101), (002), (102), (201), (202), (113), (104), (204) and (006), respectively. Furthermore, the top three strong peaks arising from (202), (201), and (102) reveal that the crystallization orientation is in the *a*-*c* plane.

We then used Raman spectroscopy as a complementary tool to XRD to further confirm the phase purity of the $Cs_3Bi_2Br_9$ and Cs_3BiBr_6 NCs. As shown in Fig. 2e, f, a typical feature of both spectra is that they each consist of two groups of bands in the high-frequency range ($V > 130$ cm^{-1}) and in the low-frequency range ($V < 100$ cm^{-1}). The Raman spectrum of $Cs_3Bi_2Br_9$ NCs shows intense sharp peaks at 191 and 165 cm^{-1}, corresponding to the two characteristic A_{1g} and E_g normal modes of Bi–Br vibrations in the corner-sharing $[BiBr_6]^{3-}$ octahedron. This finding agrees very well with the $Cs_3Bi_2Br_9$ film prepared by physical vapor deposition and with the $Cs_3Bi_2Br_9$ single crystal [23,42]. For Cs_3BiBr_6 NCs, the Raman spectrum shows broad peaks at 159 and 133 cm^{-1}, with a red-shift to lower energy (32 nm^{-1}) as compared with that of the $Cs_3Bi_2Br_9$ NCs, indicating the weaker Bi–Br bonds in Cs_3BiBr_6 [43]. Clearly, the Raman peak at 133 cm^{-1} for Cs_3BiBr_6 is absent in $Cs_3Bi_2Br_9$, and *vice versa*, the Raman peak at 191 cm^{-1} for $Cs_3Bi_2Br_9$ is absent in Cs_3BiBr_6. Such distinct Raman features of Cs_3BiBr_6 and $Cs_3Bi_2Br_9$ are sufficient to distinguish one from the other. Therefore, through the careful analysis of XRD and Raman results, any impurity can be firmly excluded for both Cs_3BiBr_6 and $Cs_3Bi_2Br_9$.

To determine the short-range order around the Br and Bi atoms in the Cs_3BiBr_6 and $Cs_3Bi_2Br_9$ NCs, we further performed XAS measurements by focusing on the near-edge region. Fig. 3 displays the experimental XANES profiles of Cs_3BiBr_6 (black) and $Cs_3Bi_2Br_9$ (red) at (a) the Br K edge and at (b) the Bi L_3 edge. Whereas the Bi spectra are largely featureless, the Br spectra display three distinctive features A, B, and C with some specificity ascribable to Cs_3BiBr_6 or $Cs_3Bi_2Br_9$. While the intensity of A is larger for $Cs_3Bi_2Br_9$ compared with Cs_3BiBr_6, the intensity of the white line feature B is larger for Cs_3BiBr_6 compared with $Cs_3Bi_2Br_9$. Feature C has an underlying fine structure indicated by the two vertical bars. The traces simulated with the FDMNES software based on the crystallographic structures determined above are shown in Fig. 3c, d. They are in good qualitative agreement with the experimental profiles. In particular, the three features A, B, and C are apparent, with a comparable lower intensity of the white line (B) in $Cs_3Bi_2Br_9$ along with the underlying structure of C indicated by the two vertical bars. A detailed assignment of A, B, and C will be described elsewhere in

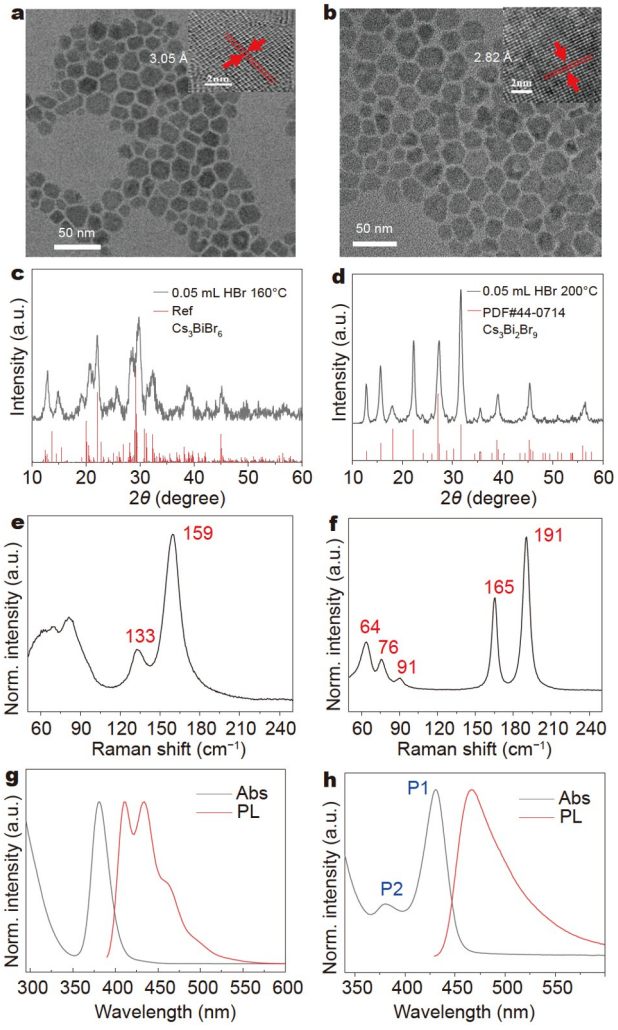

Figure 2 TEM images of the obtained (a) Cs_3BiBr_6 NCs along with the size distribution of 13.2 ± 0.29 nm (see Fig. S3a) and (b) $Cs_3Bi_2Br_9$ NCs along with the size distribution of 16.0 ± 0.24 nm (see Fig. S3b). The inset shows the HRTEM. XRD patterns of the as-prepared (c) Cs_3BiBr_6 and (d) $Cs_3Bi_2Br_9$ NCs. Raman spectra of (e) Cs_3BiBr_6 and (f) $Cs_3Bi_2Br_9$ NCs. UV-vis and PL spectra of (g) Cs_3BiBr_6 and (h) $Cs_3Bi_2Br_9$ NCs excited with 360 nm.

connection with the interpretation of time-resolved pump-probe XAS measurements in our upcoming publication. Overall, as with the techniques that characterize the long-range order employed above (XRD and Raman), the two materials with different stoichiometries are also distinguishable based on their XANES profiles that are sensitive to the local order.

Secondly, we investigated the steady-state optical properties of the as-synthesized Cs_3BiBr_6 with a mean particle size of 13.23 ± 0.29 nm and $Cs_3Bi_2Br_9$ NCs with a mean particle size of 16.00 ± 0.24 nm. Fig. 2g shows the UV-vis absorption and PL spectra of the Cs_3BiBr_6 NCs. The absorption band shows a sharp exciton absorption peak at 380 nm in the UV region. By analogy, we propose that the products exhibiting an absorption peak at ~380 nm reported in the previous work [36] are also Cs_3BiBr_6 NCs, rather than $Cs_3Bi_2Br_9$ NCs. The PL spectrum of Cs_3BiBr_6 NCs excited with 360 nm shows two emission peaks at 410 and 434 nm in the deep blue region, and a shoulder at 460 nm, which could originate from different charge carrier radiative recombination paths involving simultaneously direct and indirect band gap transitions, or states below the edge [44]. For comparison, the UV-vis absorption and PL spectra excited with 360 nm of $Cs_3Bi_2Br_9$ NCs are shown in Fig. 2h. The UV-vis absorption shows two peaks: a sharp one between 430 and 440 nm (P1), and a weak one at the wavelength shorter than 400 nm (P2). The PL spectrum shows an emission peak at 466 nm with a full-width-at-half-maximum (FWHM) of ~55 nm, which has a small Stokes shift of 36 nm (Fig. 2h). In addition, a long tail on the low energy side is observed in the PL spectrum, indicating an indirect transition or states below the band gap [45]. The absolute PLQY of 26.7% was obtained using an FLS 920P steady-state/transient fluorescence spectrometer equipped with an integrating sphere. This value is relatively high compared with the previously reported results coming from the emission of single exciton recombination, which will be discussed later with the transient optical spectra.

To further analyze the sensitivity of the absorption spectra of $Cs_3Bi_2Br_9$ NCs systematically, we prepared $Cs_3Bi_2Br_9$ NCs with varied sizes and morphologies. We change the amount of OA, the reaction time, and the centrifugation speed while keeping the temperature at 200°C to get products of various sizes and morphologies. Fig. 2b and Fig. 4d show the bright field TEM images of the $Cs_3Bi_2Br_9$ NCs prepared with 1 and 5 mL OA, respectively, at the same temperature (200°C). As shown clearly, they both have a hexagonal shape in the *a*-*c* plane, and their average crystal size is very close, 16.00 ± 0.24 nm for 1 mL OA, and 17.15 ± 0.17 nm for 5 mL OA. However, the sample prepared with 5 mL OA shows many differently oriented lattice planes (see Fig. 4d). We also compare their XRD and find that the intensity of the peak at 18.009° corresponding to (002) with 5 mL OA far outweighs its counterpart with 1 mL OA (see Fig. 4g). On the contrary, the intensity of the peak at 22.189° corresponding to (102) is exactly reversed. Both TEM and XRD results indicate that OA promotes the growth of $Cs_3Bi_2Br_9$ NCs along the *c* axis. From the UV-vis absorption spectra shown in Fig. 4a, we can see that the peak P2 of the sample with *c*-axis orientation becomes extremely weak and redshifted. Therefore, P2 is tightly linked to the preferred crystallographic orientation.

We also studied the impact of the average crystal size on the UV-vis absorption spectrum of $Cs_3Bi_2Br_9$ NCs. The average sizes of the NCs were modified by controlling the centrifugation speed. NCs of 18.12 ± 0.37 nm were obtained with a centrifugation speed of 7000 r min^{-1} (see Fig. 4e), while 34.12 ± 1.21 nm-sized NCs were obtained with a centrifugation speed of 500 r min^{-1} (see Fig. 4f). Their UV-vis absorption spectra (Fig. 4b) show that the peak P2 disappeared with increasing NC size, indicating the crystal size dependence of this peak. It has been suggested that the peak P2 probably originates from $[BiBr_6]^{3-}$ in solution, $[BiBr_6]^{3-}$ complexed with ligands used in synthesis, or Cs_3BiBr_6 NCs rather than the product $Cs_3Bi_2Br_9$, as $[BiBr_6]^{3-}$ may always be present in solution synthesis and colloidal dispersions [42]. In our experiments, the Cs_3BiBr_6 NCs can be excluded by the analysis of the Raman spectra. Since the only difference between the two samples with and without P2 is their particle size, possible impurities from $[BiBr_6]^{3-}$ complexed with ligands can also be ruled out. Therefore, our results prove that the peak P2 comes precisely from the $Cs_3Bi_2Br_9$ product, rather than any other impurities. Moreover, this peak is unambiguously related to the average size and crystallographic orientation of the NCs. For the peak P1, it has been widely thought to arise from the $1S_0 \rightarrow 3P1$ transition of a $[BiBr_6]^{3-}$

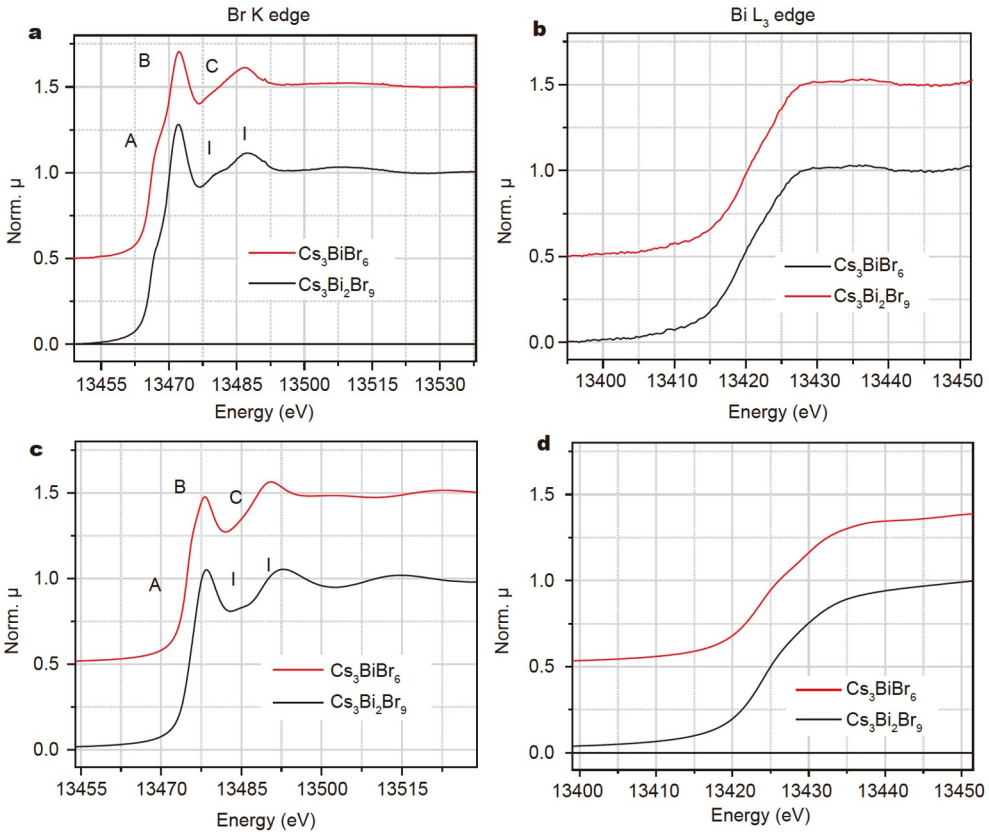

Figure 3 Experimental XANES profiles for Cs_3BiBr_6 (black) and $Cs_3Bi_2Br_9$ (red) at the (a) Br K edge and (b) Bi L_3 edge. Simulated XANES profiles for Cs_3BiBr_6 (black) and $Cs_3Bi_2Br_9$ (red) at the (c) Br K edge and (d) Bi L_3 edge.

octahedron, which has molecule-like characteristics and is size-independent [20,46,47]. However, in our measurements, the peak P1 redshifts with increasing crystal size, suggesting that it is also size dependent. This conclusion is also confirmed by another set of experimental results shown in Fig. 4c. By increasing the reaction time to 30 min, we obtained small NCs with a mean particle size of 20.12 ± 0.21 nm at 7000 r min^{-1} and large NCs with a mean particle size of 49.58 ± 0.94 nm at 500 r min^{-1} centrifugation speed (see Fig. S4). The relationship between the peak P1 and the average crystal size follows the trend identified above. Therefore, the peak P1 of $Cs_3Bi_2Br_9$ NCs is not from the $1S_0 \rightarrow 3P_1$ transition of $[BiBr_6]^{3-}$ octahedron. Referring to previous studies on $CsPbBr_3$ NCs [48,49], generally, P1 and P2 can be assigned to transitions from the first and second hole levels in the valence band to the first and second electron levels in the conduction band, namely, the absorption of the first exciton and second exciton, respectively [50]. Our experimental result matches well with the calculated absorption spectrum for $Cs_3Bi_2Br_9$ [30].

Having established the conditions for synthesizing phase-pure $Cs_3Bi_2Br_9$ NCs (parameters: 200°C, 1 mL OA, reaction time 10 s, centrifugation 7000 r min^{-1}, and average size: 16.00 ± 0.24 nm), we then investigated their photoinduced charge carrier dynamics by fs-TA measurements with various pump fluences (see Table S2 and Fig. S5). The details of the pump-probe TA setup can be found in the characterization section of the Supplementary information. Fig. 5 presents the pseudo-color fs-TA map for the $Cs_3Bi_2Br_9$ NCs pumped at 340 nm with an incident fluence of 1.65 × 10^{14} photons $pulse^{-1}$ cm^{-2} and the globally fitted exponential decay-associated spectral (DAS) components from the global fit analysis. The pseudocolor TA plot features three bands (see Fig. 5a): the negative signal near the bandgap at 430 nm associated with ground state bleaching (GSB); the photoinduced absorption above the bandgap at 396 nm (PIA1) attributed to band filling, and, partially, to a transient change in refractive index with excess carrier concentrations in film samples [51,52]; and the photoinduced absorption below the bandgap at 454 nm (PIA2) due to bandgap renormalization, where the carrier-driven electric fields reduce the bandgap [53]. The buildup of the GSB signal grows with the decay of PIA1 and carries information about the hot carrier cooling process [54]. Note that the GSB signal takes a longer time to reach the maximum with increasing pump fluence (see Fig. 5d), indicating a longer lifetime of the hot carriers. Recombination through several channels starts dominating once the GSB reaches the maximum. Intriguingly, the global fitting delivers three decay components (see Fig. 5b). The ultrafast decay component with a lifetime of ~3 ps is assigned to the formation of the self-trapped exciton [25,55]. Its rate does not vary with the laser fluence (see Table S2 and Fig. S6a). The lifetime of the second component is around 100 ps. It is attributed to multiple-exciton decay dynamics that is highly dependent on the number of initially generated electron-hole (e-h) pairs. This process is important in the present NCs considering the high value of the initial average number of e-h pairs per nanoparticle after photoexcitation $\langle N \rangle$ ~3.98 ($\langle N \rangle = J_0 \times \sigma$, evaluated from the excitation intensity J_0 and absorption cross section σ of the NCs, see calculation of carrier density in Supplementary information and Fig. S7). The

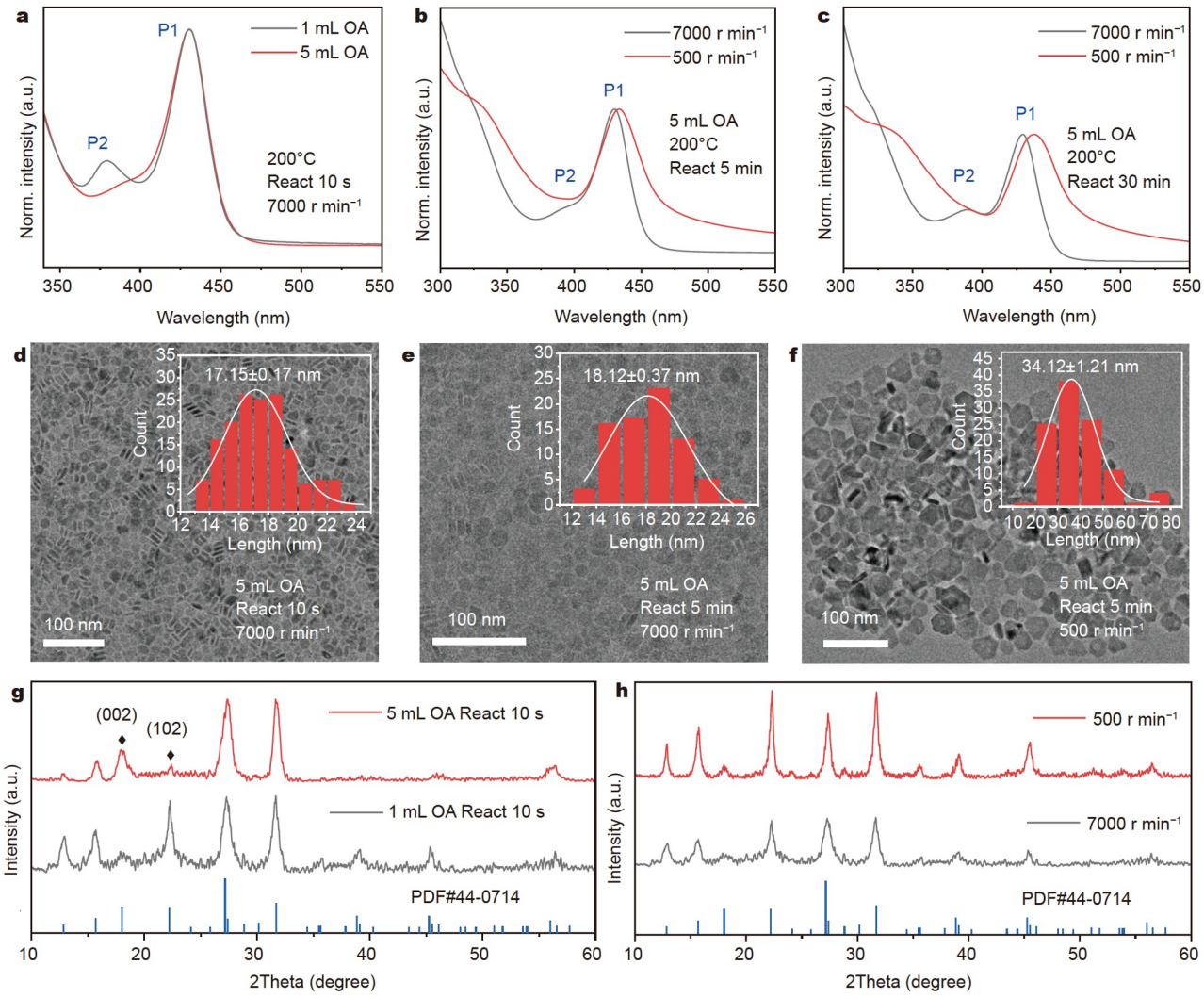

Figure 4 (a–c) UV-vis absorption of the as-prepared $Cs_3Bi_2Br_9$ NCs under different experimental parameters. TEM images of the $Cs_3Bi_2Br_9$ NCs prepared with (d) 5 mL OA, reaction time of less than 10 s, and centrifugation speed of 7000 r min^{-1}; (e) 5 mL OA, reaction time of 5 min, and centrifugation speed of 7000 r min^{-1}; and (f) 5 mL OA, reaction time of 5 min, and centrifugation speed of 500 r min^{-1}. (g) XRD of $Cs_3Bi_2Br_9$ NCs prepared with 1 and 5 mL OA, reaction time of less than 10 s, and centrifugation speed of 7000 r min^{-1}. (h) XRD of $Cs_3Bi_2Br_9$ NCs with 5 mL OA, reaction time of 5 min, and centrifugation speeds of 7000 and 500 r min^{-1}.

rate of the second component becomes faster with increasing pump fluence, and is proportional to $1/J_0$ (see Fig. S6b). Finally, the long-lived component with a lifetime greater than 2 ns is assigned to the single-exciton recombination. Its rate also becomes faster with increasing pump fluence, which is in line with the published results on Pb-based and Bi-based perovskite materials (Fig. S6c) [56,57]. We also measured the PL decay of $Cs_3Bi_2Br_9$ NCs with TCSPC, as shown in Fig. S8. The curve was fitted by a bi-exponential function with a short-lived component (τ_1 < 1 ns) and a long-lived component (τ_2 ~4.8 ns). Particularly, the value of the long-lived component is well consistent with the third component of the TA result, confirming that this process is emissive single-exciton recombination.

The photostability of the perovskite NCs is a critical factor for their long-term operation in functioning devices. We prepared $Cs_3Bi_2Br_9$ NCs both by our new MHI and the LARP methods. Photostability tests of the perovskite NCs were all done under ambient conditions. The colloidal NC solution was put in quartz cuvettes (1 mm) and then a continuous laser (405 nm, 10 mW cm^{-2}) was used to irradiate the sample in the cuvettes for a certain time. The LARP method for preparing $Cs_3Bi_2Br_9$ NCs has been described elsewhere [58]. As shown in Fig. S9, the MHI-sample exhibits astonishing stability after 4 h of laser exposure, and their UV-vis absorption spectra display no apparent change. In contrast, the LARP-sample suffers severe photodegradation after only 30 min of irradiation with an even much lower laser flux of 1 mW cm^{-2}, as their color changed from yellowish green to colorless. We note that the UV-vis absorption spectra of the LARP-sample display only the peak P1 between 430 and 440 nm. We checked the Raman spectrum of the LARP-sample and found that it is completely identical to that of the MHI-sample (see Fig. S10c), indicating that their crystal structures are the same. Then we examined the morphology of the sample prepared by the LARP method and found that large crystals of tens to 200 nm are always present together with small NCs of 4 nm (see Fig. S10a, b). This is the reason why the peak P2 located at a wavelength shorter than 400 nm disappears in the UV-vis absorption spectrum of the LARP-sample.

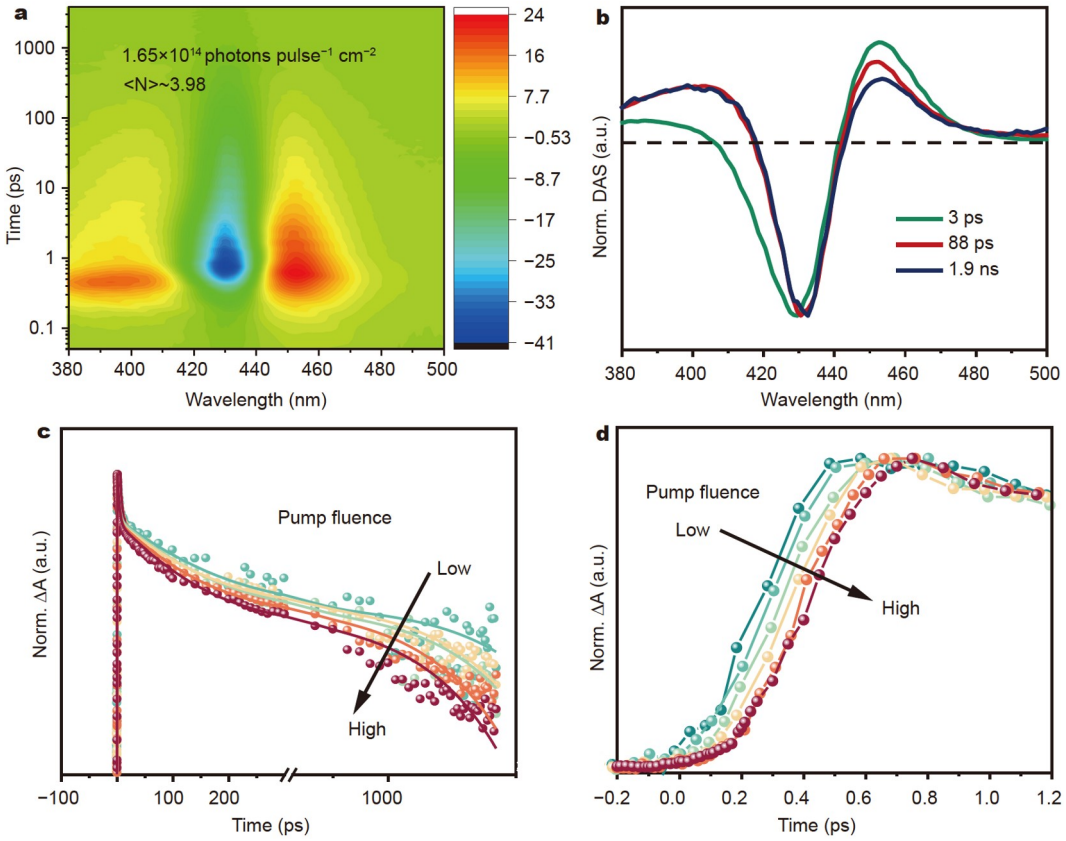

Figure 5 Results of the TA measurements of colloidal $Cs_3Bi_2Br_9$ NCs. (a) Pseudo-color TA plot pumped at 340 nm with a pump flux of 1.65 × 10^{14} photons $pulse^{-1}$ cm^{-2}, and the corresponding e-h pair of <*N*> ~3.98. (b) DAS components, obtained from a triexponential global-fit model GSB decay dynamics within a full-time range (c) and at an early time (d) probed at 430 nm under the laser pump flux from 5.23 × 10^{13} to 1.65 × 10^{14} photons $pulse^{-1}$ cm^{-2}.

In addition, bismuth perovskite NCs with other halide compositions ($Cs_3Bi_2X_9$, X = Cl, I) can also be successfully synthesized by our MHI method using different Bi halides (see the Supplementary information for details). The as-synthesized $Cs_3Bi_2X_9$ (X = Cl, Br, I) NCs show color changes from colorless to red when the halide is varied from Cl to I, as shown in Fig. S11. The UV-vis absorption spectra of the NCs show sharp peaks in the range from 332 to 492 nm (Fig. S11). We checked the morphologies and structures of these NCs by TEM and XRD (see Fig. S12), and found that the Cl-based perovskite presents nanospherical morphology with an average size of 17.84 ± 0.41 nm, while in contrast, the I-based perovskite has a nano-hexagonal plate morphology with a mean particle size of 21.31 ± 0.40 nm. The XRD pattern shows that they have a preferred orientation of (001) and belong to the hexagonal space group $P6_3/mmc$. Therefore, the MHI method developed in this work is universal for the large-scale synthesis of photostable bismuth perovskite NCs with tunable composition, optical band gap, and emission color.

Finally, to evaluate the optoelectronic performance of our photostable MHI bismuth perovskite NCs and to demonstrate their practical relevance for fully functional devices, we fabricated a photodetector based on the $Cs_3Bi_2Br_9$ NCs and measured its photoresponse. The structure and the energy diagram of the photodetector are shown in Fig. 6a, b, respectively. The advantage of colloidal NCs is that they can be deposited from the solution without complicated setups and processes. The colloidal NCs were spin-coated directly on PEDOT:PSS deposited on a pre-patterned ITO substrate, and the morphology was characterized with the scanning electron microscopy (SEM). The SEM image in Fig. S13 shows the typical flat morphology and uniform size of the NCs on the substrate. The photoresponse properties were characterized under a bias voltage of 1 V. A sharp current increase was observed in the presence of 405-nm laser illumination (2 mW cm^{-2}). The value of the photocurrent enhancement, i.e., the ratio of I_{Photo}/I_{Dark}, was found to be ~43, which is not very high but still comparable to most of the lead-free perovskite-based photodetectors. The key reason is that we did not modify the device structure, including the selection of carrier transporting materials and optimization of interfaces between different layers. In general, enhancing the light capture and improving the carrier transport of the perovskite active layer as well as the crystal quality of the NCs could get a higher on-off ratio [59]. For example, Sun *et al.* [60] integrated gold nanoparticles underneath the graphene, where the plasmonic effect of gold nanoparticles can substantially enhance the near-field of perovskite and facilitate the light-harvesting efficiency, thus the responsivity of the photodetector was doubly enhanced; by doping Zn^+ to the $CsPbBr_3$ active layer to improve the quality of the NCs and reduce the defects, Wang *et al.* [61] enhanced the on-off ratio by ~13 times. Therefore, with further optimization of the device structure, contacting interfaces, and crystal quality of the $Cs_3Bi_2Br_9$ NCs, etc., it would be possible to substantially improve the performance of the photodetector with high pho-

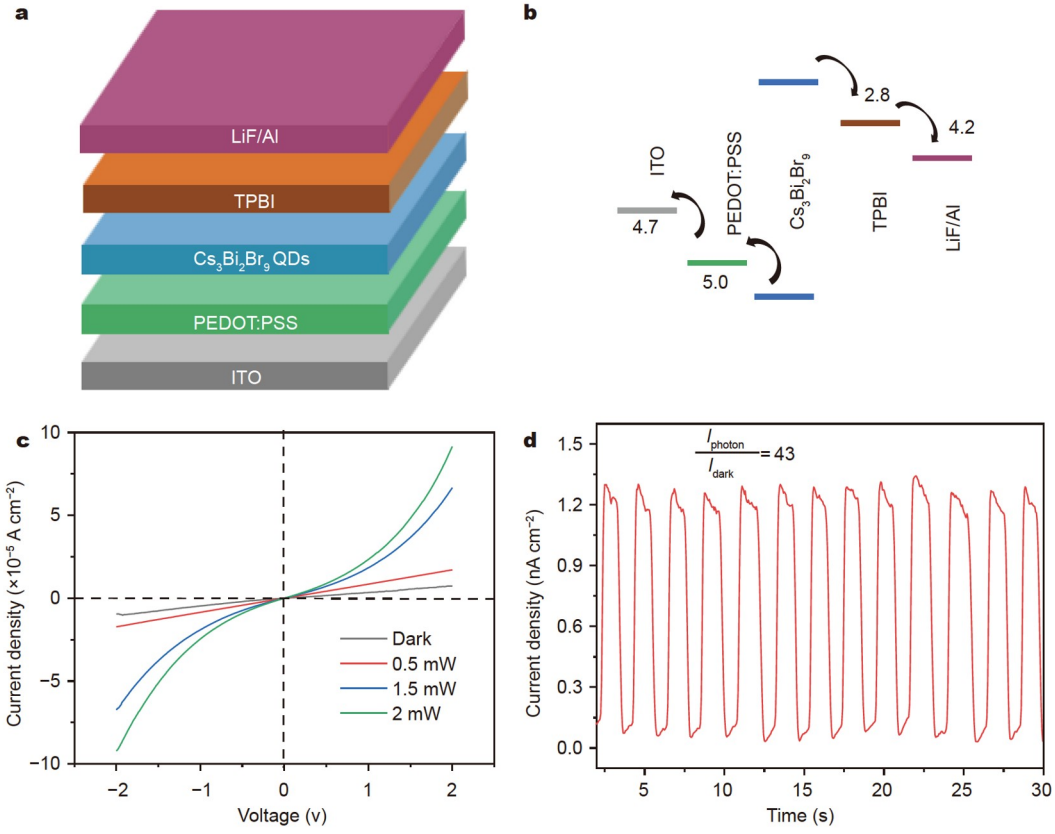

Figure 6 (a) Device structure and (b) energy diagram of the $Cs_3Bi_2Br_9$ NCs-based photodetector. (c) Current density-voltage curves under different illumination powers. (d) The current density-time curve of the $Cs_3Bi_2Br_9$ NCs-based photodetector at a bias voltage of 1 V, where the illumination laser power is 10 mW cm^{-2}.

tostability.

CONCLUSIONS

We report a universal MHI method for the synthesis of highly photostable lead-free bismuth-based perovskite NCs with controllable particle size while retaining excellent phase purity. The crystal structure and chemical composition of the NCs can be easily controlled by changing the hot injection temperature. We obtain pure Cs_3BiBr_6 NCs at the temperature between 160 and 180°C and pure $Cs_3Bi_2Br_9$ NCs at the temperature between 200 and 240°C. The UV-vis absorption spectra of the $Cs_3Bi_2Br_9$ NCs feature two peaks. The peak P1 at the wavelength between 430 and 440 nm only shows redshift with increasing NC size; while the peak P2 at the wavelength shorter than 400 nm is tightly related to both NC size and morphology, which becomes weaker and shows redshift in the sample with the (001) preferred orientation, and finally disappears with increasing NC size. P1 and P2 can be assigned to absorption of the first exciton and second exciton, respectively. Our results ultimately clarify the controversy on the absorption peaks of the previously reported bismuth perovskite NCs. The fs-TA measurements on the as-synthesized $Cs_3Bi_2Br_9$ NCs reveal that the excited charge carriers recombine through three different channels: the ultrafast one of ~3 ps due to the carrier self-trapping process, the second one of ~100 ps associated with the multiple-exciton recombination and the long-lived one of >2 ns stemming from the single-exciton recombination. Moreover, the as-prepared $Cs_3Bi_2Br_9$ NCs with the MHI method show superior photostability compared with those prepared by the LARP method, and the photodetector based on our $Cs_3Bi_2Br_9$ NCs shows excellent performance with an on/off ratio of ~43, demonstrating the potential of the $Cs_3Bi_2Br_9$ NCs in optoelectronic applications.

Received 29 August 2022; accepted 24 October 2022; published online 5 January 2023

1 Dey A, Ye J, De A, *et al.* State of the art and prospects for halide perovskite nanocrystals. ACS Nano, 2021, 15: 10775–10981
2 Liu XK, Xu W, Bai S, *et al.* Metal halide perovskites for light-emitting diodes. Nat Mater, 2021, 20: 10–21
3 Wang X, Bao Z, Chang YC, *et al.* Perovskite quantum dots for application in high color gamut backlighting display of light-emitting diodes. ACS Energy Lett, 2020, 5: 3374–3396
4 Wang HC, Bao Z, Tsai HY, *et al.* Perovskite quantum dots and their application in light-emitting diodes. Small, 2018, 14: 1702433
5 Green MA, Ho-Baillie A, Snaith HJ. The emergence of perovskite solar cells. Nat Photon, 2014, 8: 506–514
6 Rong Y, Hu Y, Mei A, *et al.* Challenges for commercializing perovskite solar cells. Science, 2018, 361: eaat8235
7 Xu X, Qian W, Xiao S, *et al.* Halide perovskites: A dark horse for direct X-ray imaging. EcoMat, 2020, 2: 1
8 Bera D, Qian L, Tseng TK, *et al.* Quantum dots and their multimodal applications: A review. Materials, 2010, 3: 2260–2345
9 Wei H, Fang Y, Mulligan P, *et al.* Sensitive X-ray detectors made of methylammonium lead tribromide perovskite single crystals. Nat Photon, 2016, 10: 333–339
10 Akkerman QA, Rainò G, Kovalenko MV, *et al.* Genesis, challenges and opportunities for colloidal lead halide perovskite nanocrystals. Nat Mater, 2018, 17: 394–405

11 Song J, Li J, Li X, *et al.* Quantum dot light-emitting diodes based on inorganic perovskite cesium lead halides ($CsPbX_3$). Adv Mater, 2015, 27: 7162–7167
12 Li X, Wu Y, Zhang S, *et al.* $CsPbX_3$ quantum dots for lighting and displays: Room-temperature synthesis, photoluminescence superiorities, underlying origins and white light-emitting diodes. Adv Funct Mater, 2016, 26: 2435–2445
13 Lin J, Lai M, Dou L, *et al.* Thermochromic halide perovskite solar cells. Nat Mater, 2018, 17: 261–267
14 Nedelcu G, Protesescu L, Yakunin S, *et al.* Fast anion-exchange in highly luminescent nanocrystals of cesium lead halide perovskites ($CsPbX_3$, X = Cl, Br, I). Nano Lett, 2015, 15: 5635–5640
15 Conings B, Drijkoningen J, Gauquelin N, *et al.* Intrinsic thermal instability of methylammonium lead trihalide perovskite. Adv Energy Mater, 2015, 5: 1500477
16 Babayigit A, Ethirajan A, Muller M, *et al.* Toxicity of organometal halide perovskite solar cells. Nat Mater, 2016, 15: 247–251
17 Jellicoe TC, Richter JM, Glass HFJ, *et al.* Synthesis and optical properties of lead-free cesium tin halide perovskite nanocrystals. J Am Chem Soc, 2016, 138: 2941–2944
18 Stoumpos CC, Frazer L, Clark DJ, *et al.* Hybrid germanium iodide perovskite semiconductors: Active lone pairs, structural distortions, direct and indirect energy gaps, and strong nonlinear optical properties. J Am Chem Soc, 2015, 137: 6804–6819
19 McCall KM, Stoumpos CC, Kostina SS, *et al.* Strong electron-phonon coupling and self-trapped excitons in the defect halide perovskites $A_3M_2I_9$ (A = Cs, Rb; M = Bi, Sb). Chem Mater, 2017, 29: 4129–4145
20 Zhou L, Xu YF, Chen BX, *et al.* Synthesis and photocatalytic application of stable lead-free $Cs_2AgBiBr_6$ perovskite nanocrystals. Small, 2018, 14: 1703762
21 Jin Z, Zhang Z, Xiu J, *et al.* A critical review on bismuth and antimony halide based perovskites and their derivatives for photovoltaic applications: Recent advances and challenges. J Mater Chem A, 2020, 8: 16166–16188
22 Lian L, Zhai G, Cheng F, *et al.* Colloidal synthesis of lead-free all-inorganic cesium bismuth bromide perovskite nanoplatelets. CrystEngComm, 2018, 20: 7473–7478
23 Bator G, Baran J, Jakubas R, *et al.* Raman studies of structural phase transition in $Cs_3Bi_2Br_9$. Vibal Spectr, 1998, 16: 11–20
24 Deng F, Zhang J, Wu S, *et al.* Growth and optical properties of lead-free $Cs_3Bi_2Br_9$ perovskite microplatelets. Phys Status Solidi (B), 2022, 259: 2100593
25 Yang B, Chen J, Hong F, *et al.* Lead-free, air-stable all-inorganic cesium bismuth halide perovskite nanocrystals. Angew Chem, 2017, 129: 12645–12649
26 Zhang Y, Yin J, Parida MR, *et al.* Direct-indirect nature of the bandgap in lead-free perovskite nanocrystals. J Phys Chem Lett, 2017, 8: 3173–3177
27 Li X, Zhang P, Hua Y, *et al.* Ultralow detection limit and robust hard X-ray imaging detector based on inch-sized lead-free perovskite $Cs_3Bi_2Br_9$ single crystals. ACS Appl Mater Interfaces, 2022, 14: 9340–9351
28 Dai Y, Tüysüz H. Rapid acidic media growth of $Cs_3Bi_2Br_9$ halide perovskite platelets for photocatalytic toluene oxidation. Sol RRL, 2021, 5: 2100265
29 Kim SY, Park DA, Park NG. Synthetic powder-based thin (<0.1 μm) $Cs_3Bi_2Br_9$ perovskite films for air-stable and viable resistive switching memory. ACS Appl Electron Mater, 2022, 4: 2388–2395
30 Bass KK, Estergreen L, Savory CN, *et al.* Vibronic structure in room temperature photoluminescence of the halide perovskite $Cs_3Bi_2Br_9$. Inorg Chem, 2017, 56: 42–45
31 Creutz SE, Liu H, Kaiser ME, *et al.* Structural diversity in cesium bismuth halide nanocrystals. Chem Mater, 2019, 31: 4685–4697
32 Leng M, Yang Y, Zeng K, *et al.* All-inorganic bismuth-based perovskite quantum dots with bright blue photoluminescence and excellent stability. Adv Funct Mater, 2018, 28: 1704446
33 Cao Y, Zhang Z, Li L, *et al.* An improved strategy for high-quality cesium bismuth bromine perovskite quantum dots with remarkable electrochemiluminescence activities. Anal Chem, 2019, 91: 8607–8614
34 Lou Y, Fang M, Chen J, *et al.* Formation of highly luminescent cesium bismuth halide perovskite quantum dots tuned by anion exchange. Chem Commun, 2018, 54: 3779–3782
35 Yang H, Cai T, Liu E, *et al.* Synthesis and transformation of zero-dimensional Cs_3BiX_6 (X = Cl, Br) perovskite-analogue nanocrystals. Nano Res, 2020, 13: 282–291
36 Nelson RD, Santra K, Wang Y, *et al.* Synthesis and optical properties of ordered-vacancy perovskite cesium bismuth halide nanocrystals. Chem Commun, 2018, 54: 3640–3643
37 Protesescu L, Yakunin S, Bodnarchuk MI, *et al.* Nanocrystals of cesium lead halide perovskites ($CsPbX_3$, X = Cl, Br, and I): Novel optoelectronic materials showing bright emission with wide color gamut. Nano Lett, 2015, 15: 3692–3696
38 Wang A, Yan X, Zhang M, *et al.* Controlled synthesis of lead-free and stable perovskite derivative Cs_2SnI_6 nanocrystals *via* a facile hot-injection process. Chem Mater, 2016, 28: 8132–8140
39 Lee D, Kim MH, Woo HY, *et al.* Heating-up synthesis of cesium bismuth bromide perovskite nanocrystals with tailored composition, morphology, and optical properties. RSC Adv, 2020, 10: 7126–7133
40 Tang Y, Liang M, Chang B, *et al.* Lead-free double halide perovskite Cs_3BiBr_6 with well-defined crystal structure and high thermal stability for optoelectronics. J Mater Chem C, 2019, 7: 3369–3374
41 Momma K, Izumi F. *VESTA 3* for three-dimensional visualization of crystal, volumetric and morphology data. J Appl Crystlogr, 2011, 44: 1272–1276
42 Tran MN, Cleveland IJ, Aydil ES. Resolving the discrepancies in the reported optical absorption of low-dimensional non-toxic perovskites, $Cs_3Bi_2Br_9$ and Cs_3BiBr_6. J Mater Chem C, 2020, 8: 10456–10463
43 Leng M, Yang Y, Chen Z, *et al.* Surface passivation of bismuth-based perovskite variant quantum dots to achieve efficient blue emission. Nano Lett, 2018, 18: 6076–6083
44 Gao M, Zhang C, Lian L, *et al.* Controlled synthesis and photostability of blue emitting $Cs_3Bi_2Br_9$ perovskite nanocrystals by employing weak polar solvents at room temperature. J Mater Chem C, 2019, 7: 3688–3695
45 Wang T, Daiber B, Frost JM, *et al.* Indirect to direct bandgap transition in methylammonium lead halide perovskite. Energy Environ Sci, 2017, 10: 509–515
46 Bai T, Yang B, Chen J, *et al.* Efficient luminescent halide quadruple-perovskite nanocrystals *via* trap-engineering for highly sensitive photodetectors. Adv Mater, 2021, 33: 2007215
47 Liu Z, Bekenstein Y, Ye X, *et al.* Ligand mediated transformation of cesium lead bromide perovskite nanocrystals to lead depleted Cs_4PbBr_6 nanocrystals. J Am Chem Soc, 2017, 139: 5309–5312
48 Rossi D, Wang H, Dong Y, *et al.* Light-induced activation of forbidden exciton transition in strongly confined perovskite quantum dots. ACS Nano, 2018, 12: 12436–12443
49 Li Y, Lai R, Luo X, *et al.* On the absence of a phonon bottleneck in strongly confined $CsPbBr_3$ perovskite nanocrystals. Chem Sci, 2019, 10: 5983–5989
50 Akkerman QA, Nguyen TPT, Boehme SC, *et al.* Controlling the nucleation and growth kinetics of lead halide perovskite quantum dots. Science, 2022, 377: 1406–1412
51 Price MB, Butkus J, Jellicoe TC, *et al.* Hot-carrier cooling and photoinduced refractive index changes in organic-inorganic lead halide perovskites. Nat Commun, 2015, 6: 8420
52 Tamming RR, Butkus J, Price MB, *et al.* Ultrafast spectrally resolved photoinduced complex refractive index changes in $CsPbBr_3$ perovskites. ACS Photonics, 2019, 6: 345–350
53 Nah S, Spokoyny BM, Soe CMM, *et al.* Ultrafast imaging of carrier cooling in metal halide perovskite thin films. Nano Lett, 2018, 18: 1044–1048
54 Chen J, Messing ME, Zheng K, *et al.* Cation-dependent hot carrier cooling in halide perovskite nanocrystals. J Am Chem Soc, 2019, 141: 3532–3540
55 Stoumpos CC, Soe CMM, Tsai H, *et al.* High members of the 2D Ruddlesden-Popper halide perovskites: Synthesis, optical properties, and solar cells of $(CH_3(CH_2)_3NH_3)_2(CH_3NH_3)_4Pb_5I_{16}$. Chem, 2017, 2: 427–440
56 Alvarez SLG, Riel CB, Madani M, *et al.* Morphology-dependent one-

and two-photon absorption properties in blue emitting $CsPbBr_3$ nanocrystals. J Phys Chem Lett, 2022, 13: 4897–4904
57 Yang B, Han K. Charge-carrier dynamics of lead-free halide perovskite nanocrystals. Acc Chem Res, 2019, 52: 3188–3198
58 Liu C, Wang Y, Geng H, *et al.* Asynchronous photoexcited electronic and structural relaxation in lead-free perovskites. J Am Chem Soc, 2019, 141: 13074–13080
59 Dong Y, Zou Y, Song J, *et al.* Recent progress of metal halide perovskite photodetectors. J Mater Chem C, 2017, 5: 11369–11394
60 Sun Z, Aigouy L, Chen Z. Plasmonic-enhanced perovskite-graphene hybrid photodetectors. Nanoscale, 2016, 8: 7377–7383
61 Wang T, Fang T, Li X, *et al.* Controllable transient photocurrent in photodetectors based on perovskite nanocrystals *via* doping and interfacial engineering. J Phys Chem C, 2021, 125: 5475–5484

Acknowledgements We thank Dr. Sergiu Levcenco for his careful proofreading of the manuscript and valuable comments. This work was supported by the National Key Research and Development Program of China (2020YFA0309300), the Natural Science Foundation of Tianjin (20JCZDJC00560 and 20JCJQJC00210), the National Natural Science Foundation of China (NSFC, 11974191 and 12127803), the 111 Project (B07013), and the "Fundamental Research Funds for the Central Universities", Nankai University (91923139, 63213040, C029211101, C02922101, and ZB22000104). We acknowledge DESY (Hamburg, Germany), a member of the Helmholtz Association HGF, for the provision of experimental facilities. Parts of this research were carried out at Petra III beamline P64. Lin W and Zou X acknowledge the Chinese Scholarship Council for their PhD scholarship.

Author contributions Fu X and Geng HF conceived the research project. Geng HF, Huang Z, Geng HX, Liu S, Naumova MA, Salvia R, Chen S, and Wei J did the experimental measurements. Zhang L did the computation. Geng HF and Huang Z proceeded with data analysis and wrote the manuscript with input from Fu X and Canton SE. All the authors contributed to the discussion and revision of the manuscript.

Conflict of interest The authors declare that they have no conflict of interest.

Supplementary information Experimental details and supporting data are available in the online version of the paper.

Huifang Geng is currently working as a postdoctoral fellow at the School of Physics, Nankai University. She obtained her PhD degree from Beihang University in 2017. She was a postdoctoral fellow at the Extreme Light Infrastructure Attosecond Light Pulse Source (ELI-ALPS), Hungary from 2017 to 2020. Her research interest includes the synthesis of metal halide perovskite nanocrystals, and their charge carrier dynamics, lattice structure dynamics, and *in-situ* stability.

Zhuanzhuan Huang is pursuing her PhD degree in condensed matter physics at the School of Physics, Nankai University. Her research interest focuses on halide perovskite quantum dots and the *in-situ* photostability of halide perovskite by 4D ultrafast electron microscopy (UEM).

Kaibo Zheng obtained his PhD degree in 2010 from the Department of Materials Science, Fudan University. Then, he joined the Chemical Physics Division at Lund University, Sweden, as a postdoctoral fellow. He is currently a senior researcher in chemical physics at Lund University and dual affiliated as a senior researcher at the Department of Chemistry, Technical University of Denmark. His research interest includes the structure and photophysics of semiconductors and perovskite quantum dots as light harvesters.

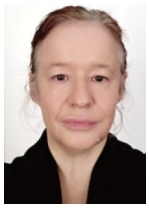

Sophie E. Canton obtained her PhD degree in 2004 from the Physics Department at Western Michigan University. Then, she joined the Chemical Physics Division at Lund University, Sweden, as a postdoctoral fellow. She is currently a visiting professor at the Department of Chemistry, Technical University of Denmark. Her research interest includes the study of photoconversion processes in molecular systems and nanomaterials for green energy production.

Xuewen Fu is a professor of physics at Nankai University. He obtained his PhD degree from Peking University in 2014. He was a postdoc in Prof. Zewail's group at Caltech from 2014–2017, followed by a research associate at Brookhaven National Laboratory from 2017–2019. His research area is 4D UEM with an emphasis on physical/chemical properties and ultrafast dynamics of low-dimensional materials by *in-situ* electron microscopy, 4D UEM, and ultrafast optical spectroscopy.

高稳定性铋基钙钛矿纳米晶的可控合成: 结构和光物理性质

耿慧芳[1†], 黄转转[1†], 耿华修[2], 刘思宇[1], Maria A Naumova[3], Raffaele Salvia[4], 陈司淇[5], 韦钧励[5], 张丽芙[1], 邹贤劭[6], 林伟华[6], 蔡欣怡[7], 袁明鉴[5], 胡振芃[1], 沈希[8], 于日成[8], 郑凯波[6,9*], Sophie E. Canton[9*], 付学文[1,10*]

摘要 铋基钙钛矿因毒性低成为铅基钙钛矿的潜在替代品. 目前, 对铋基钙钛矿纳米晶的化学组成、晶体结构以及光物理过程的研究还缺乏系统性. 特别地, 紫外-可见吸收光谱和激发态载流子动力学, 在已发表的论文中存在相当大的争议. 在本文中, 我们通过热注入法成功地合成了纯相的Cs_3BiBr_6和$Cs_3Bi_2Br_9$纳米晶, 并通过调节热注入的温度来精确控制二者的化学组成和结构. 在此基础上, 系统研究了不同形貌和不同尺寸的$Cs_3Bi_2Br_9$纳米晶的紫外-可见吸收光谱, 澄清了在这方面存在的争议. 采用飞秒瞬态吸收光谱系统研究了$Cs_3Bi_2Br_9$纳米晶的激发态载流子动力学, 结果表明载流子在被激发后的3 ps内会发生一个自捕获过程. 与配体辅助再沉积法相比, 用热注入法制备的$Cs_3Bi_2Br_9$纳米晶具有更好的光稳定性. 基于$Cs_3Bi_2Br_9$纳米晶的光电探测器具有灵敏的光响应, 显示出其在光电探测方面的应用潜力.